International Journal of Greenhouse Gas Control 33 (2015) 40–50

Contents lists available at ScienceDirect

International Journal of Greenhouse Gas Control

journal homepage: www.elsevier.com/locate/ijggc

Micro-scale CFD modeling of reactive mass transfer in falling liquid films within structured packing materials

Daniel Sebastia-Saez[a], Sai Gu[a,b,*], Panneerselvam Ranganathan[a], Konstantinos Papadikis[b]

[a] School of Energy, Environment and Agrifood, Cranfield University, Cranfield MK43 0AL, United Kingdom
[b] Department of Civil Engineering, Xi'an Jiaotong-Liverpool University, Suzhou, Jiangsu Province 215123, PR China

ARTICLE INFO

Article history:
Received 13 September 2014
Received in revised form 8 November 2014
Accepted 28 November 2014
Available online 24 December 2014

Keywords:
VOF
Structured packing
Carbon capture
CFD
Reactive mass transfer

ABSTRACT

Post-combustion carbon capture in structured packing columns is considered as a promising technology to reduce greenhouse gas (GHG) emissions because of its maturity and the possibility of being retrofitted to existing power plants. CFD plays an important role in the optimization of this technology. However, due to the current computational capacity limitations, the simulations need to be divided into three scales (i.e. micro-, meso- and macro-scale) depending on the flow characteristics to be analyzed. This study presents a 3D micro-scale approach to describe the hydrodynamics and reactive mass transfer of the CO_2-MEA chemical system within structured packing materials. Higbie's penetration theory is used to describe the mass transfer characteristics whereas enhancement factors are implemented to represent the gain in the absorption rate attributable to the chemical reaction. The results show a detrimental effect of the liquid load on the absorption rate via a decrease in the enhancement factor. The evolution of the wetted area for MEA solutions is compared to the case of pure water highlighting the differences in the transient behavior. The CO_2 concentration profiles are examined showing the capability of the model to reproduce the depletion of the solute within the bulk liquid ascribed to the high value of the Hatta number. Also, several approaches on the reaction mechanism such as reversibility and instantaneous behavior are assessed. The results from micro-scale are to be used in meso-scale analysis in future studies to optimize the reactive absorption characteristics of structured packing materials.

1. Introduction

The UK will face significant energy challenges in the near future as the electricity demand will keep escalating during the present century. Also, forecasts predict that fossil-fuels will continue to be used for power generation, with coal representing 30% of the total production (Odenberger and Johnson, 2010). Although carbon dioxide is not the greenhouse gas with the highest global warming potential (GWP), it represents the largest amount of emissions compared to other GHGs such as methane (CH_4), nitrous oxide (N_2O), and hydrofluorocarbons (HFCs). This makes carbon capture and storage (CCS) a necessity in order to decarbonize UK's economy and achieve a reduction of 80% in CO_2 emissions by 2050 with the 1990 baseline.

CCS is the industrial process that deals with the capture of CO_2 from large point sources and its transportation through pipelines to the final storage site. Several technologies exist in order to perform CO_2 capture: pre-combustion, oxy-fuel and post-combustion. In pre-combustion the fuel is previously gasified to obtain hydrogen and CO_2 as products. Thereafter, CO_2 can be separated by adsorption, absorption, membrane separation or cryogenic distillation. Hydrogen is burnt afterwards in the conventional way for energy generation (Buba et al., 2013). Oxy-fuel technology consists in burning the fuel in a pure oxygen environment. Carbon dioxide and water are thus the sole products of the reaction. The high concentration of CO_2 in the flue gases facilitates its separation. Oxy-fuel technology is especially suitable for solid fossil fuel power plants (Said et al., 2011). Post-combustion carbon capture consists on the removal of CO_2 from the flue gases after combustion. Absorption by means of chemical solvents (i.e. mainly amine solutions) in either random or structured packings is the preferred method. After its capture, the gas is transported in supercritical state due to efficiency reasons through pipelines or by shipping. CO_2 can be used to perform enhanced oil recovery (EOR) or to be permanently stored

* Corresponding author at: School of Energy, Environment and Agrifood, Cranfield University, Cranfield MK43 0AL, United Kingdom. Tel.: +44 1234 758207; fax: +44 1234 754685.
E-mail address: s.gu@cranfield.ac.uk (S. Gu).

http://dx.doi.org/10.1016/j.ijggc.2014.11.019

Nomenclature

Latin symbols

a	area per unit volume [m^{-1}]
c	molar concentration [kmol m^{-3}]
C	mass concentration [kg m^{-3}]
D	diffusion coefficient [m^2 s^{-1}]
E	enhancement factor
F	volume fraction
g	acceleration of gravity [m s^{-2}]
k	liquid side mass transfer coefficient [m s^{-1}]
K	reaction rate [m^3 $kmol^{-1}$ s^{-1}]
L	distance from liquid inlet [m]
M	Hatta number squared
P	pressure [Pa]
R	chemical consumption rate [kmol m^{-3} s^{-1}]
S	mass source term [kg m^{-3} s^{-1}]
t	time [s]
v	velocity [m s^{-1}]
y	mass fraction
z	stoichiometric coefficient MEA

Greek symbols

δ	liquid film thickness [m]
μ	dynamic viscosity [Pa s]
ρ	density [kg m^{-3}]
σ	surface tension [N m^{-1}]
τ	contact time [s]

Subscripts

∞	instantaneous reaction
CO_2	carbon dioxide
e	effective
for	forward reaction
g	gas
i	interface
l	liquid
MEA	monoethanolamine
TOT	total

Other symbols

∇	Nabla operator
Ha	Hatta number
He	Henry's law constant
We	Weber number

in saline formations or coal seams. Different trapping mechanisms include: structural and stratigraphic trapping, solubility trapping, mineral trapping and residual trapping (Fagerlund et al., 2013). Stratigraphic trapping consists in storing the carbon dioxide under low permeability layers such as caprocks or anticlines. In solubility trapping the CO_2 is dissolved in brines (i.e. water encountered in the porous rocks with a high content of salts). Mineral trapping involves chemical reactions between the acidic brines and silicate minerals to form solid carbonates. Mineral trapping has been proven to be the most stable form of trapping despite the low velocity of the chemical reaction. In residual trapping carbon dioxide blobs remain within the fluid that fills the porous media.

Chemical absorption has a big potential of being applied for carbon capture since it has been proven to be a mature technology and it has already been largely applied in the chemical industry. It has also been demonstrated to be suitable for large amounts of flue gases with a low CO_2 concentration (between 3% and 15%) as produced in natural gas combined-cycle NGCC power plants. Monoethanolamine (i.e. MEA) is the most common substance used for chemical absorption of CO_2 since it presents the advantages of enhancing the absorption process by reacting quickly with carbon dioxide; good biodegradability and low price. In opposition, it presents high risk of corrosion, especially for high concentrations. The process takes place in a continuous scrubbing device formed by two columns: absorber and stripper. The flue gas from the power plant enters the absorber and comes into contact with an aqueous amine solution. The output from the absorber is both the clean flue gas and the CO_2-rich solvent. The solution is then introduced in the stripper, where the weak chemical bonds between the CO_2 and the solution are broken by applying hot steam. Regeneration of the amine solution constitutes normally the highest energy penalty of the system; accounting for as much as 80% of the operational cost (Mores et al., 2012; Raynal et al., 2011). At the present time CCS has been successfully tested at pilot-plant scale (e.g. Boundary Dam CCS Project in Canada) but only the Shanghai Shidongkou power plant in China implements this technology at commercial scale, trapping 120,000 t of CO_2 per year (Power, 2011–07–20). Romeo et al. (2008) establish that the target total cost of CCS has to be maintained under 25 €/t CO_2 whereas nowadays it lies between 40 and 70 €/t CO_2. More research has yet to be undergone on CCS to overcome economical drawbacks and become a fully commercialized technology.

Computational studies of CO_2 capture can be performed either by means of process simulations or CFD at three different scales (i.e. including micro-, meso- and macro-scale) depending on the aspect to be studied due to current computational capacity limitations (Raynal and Royon-Lebeaud, 2007; Sun et al., 2013). The results from each particular scale can be fed to the next level. Process simulations can be used satisfactorily to check how different plant configurations can affect its overall behavior. Each component is treated as a black box and no insight about the physical and chemical phenomena therein can be reached. Computational fluid dynamics can be applied to tackle this drawback. Macro-scale simulations describe the whole reactor by comparing the structured packing to a porous medium. Liquid dispersion and the influence of geometrical features such as injectors and walls can be assessed with this approach. Meso-scale simulations are normally focused in the pressure-loss characteristics of the absorber. Structured packings are formed by a repeating geometrical unit called REU (i.e. representative elementary unit). At this scale, the computational domain consists of several REUs whose pressure loss can be correlated to the one taking place in the entire column. Micro-scale simulations consist in small computational domains (i.e. in the order of millimeters or a few centimeters). Micro-scale simulations describe the gas–liquid interfacial phenomena such as hydrodynamics (i.e. liquid misdistribution) and mass exchange. Most of the work carried out at this scale is still focused in the hydrodynamics aspects. Cooke et al. (2014) aimed to improve the description of the hydrodynamics by using local adaptive mesh refinement (AMR) at the gas–liquid interface, reducing significantly the calculation time. Table 1 summarizes the conclusions from the work carried out so far. This paper expands the previous work from the authors and aims to alleviate the lack of literature on CFD modeling of reactive mass transfer in multiphase flows.

2. Computational model

The present work uses the volume of fluid method (VOF), which implements an additional variable called volume fraction to describe the gas–liquid interface. The calculations are performed with the commercial software ANSYS® FLUENT v14.0. The finite volume method (FVM) is used to solve the Navier–Stokes equations

Table 1
Literature review.

Authors	Computational approach	Conclusions
Sebastia-Saez et al. (2013)	Micro-scale CFD	3D transient and pseudo-steady study of liquid film flows over inclined plates. Hydrodynamics and physical mass transfer validation. Effect of plate textures, liquid velocity and viscosity on the hydrodynamics.
Sebastia-Saez et al. (2014)	Micro-scale CFD	Influence of gas pressure, gas velocity, MEA contents, flow configuration and contact angles on the physical mass transfer characteristics of the O_2-aqueous MEA system.
Haroun et al. (2010)	Micro-scale CFD	Two-dimensional VOF simulation of interfacial gas–liquid reactive mass transfer. Discontinuity in the concentration profile at the interface is represented. The relation between Hatta number and the enhancement factor is benchmarked.
Haroun et al. (2014)	Meso-scale CFD	Three-dimensional VOF simulation. Focuses on hydrodynamics (i.e. liquid misdistribution) in actual sections of Mellapak 250.X, reproducing rivulet flow.
Chen et al. (2009)	Meso-scale CFD	Three dimensional VOF simulations. The work presents velocity and concentration fields in a criss-cross section of Mellapak 350.Y.
Hosseini et al. (2012)	Micro-scale CFD	Two-dimensional VOF simulation. The validity of the correlations between dry and wet pressure drops is checked.
Ahn et al. (2013)	Process simulation	Study of the influence of an intercooler between absorber and stripper. The capacity of the solvent is increased with this configuration leading to smaller equipment.
Edge et al. (2013)	Co-simulation	Heat flux data from CFD simulations are regressed as a function of the furnace height and linked to a oxy-fuel process model developed with Gproms®.
Brinkmann et al. (2014)	Co-simulation	Reactive absorption in structured packings by hydrodynamic analogy. The model is linked to an Aspen Plus™ process simulation.

(conservation of mass and momentum equations) for gas–liquid incompressible and isothermal flow.

The continuity equation writes:

$$\nabla \cdot \vec{v} = 0 \tag{1}$$

Whereas the momentum equation is:

$$\rho\left(\frac{\partial \vec{v}}{\partial t} + \vec{v}\cdot\nabla\vec{v}\right) = -\nabla P + \mu\nabla^2\vec{v} + \rho\vec{g} + \vec{f}, \tag{2}$$

The parameter $\vec{f}$ accounts for other forces different from pressure, viscosity and gravity that might act on the fluid. In this work, $\vec{f}$ accounts for the surface tension force, which is described by means of the CSF model (Brackbill et al., 1992). The values used for the surface tension are 71.01 mN m^{-1} for pure water and 48.95 mN m^{-1} for monoethanolamine. The CSF model can lead to the appearance of the so-called parasitic currents (Meier et al., 2002; Liovic and Lakehal, 2012), which are abnormal values of the velocity caused by miscalculations in the curvature term. A parabolic profile was introduced for the velocity at the gas phase inlet to avoid the effect of the parasitic currents.

The physical properties in Eq. (2) are volume fraction-averaged:

$$\rho = F\rho_l + (1-F)\rho_g \tag{3}$$

$$\mu = F\mu_l + (1-F)\mu_g \tag{4}$$

The solution for the volume fraction field can be obtained by solving its continuity equation

$$\frac{\partial F}{\partial t} + \vec{v}\cdot\nabla F = 0, \tag{5}$$

A computational cell with a volume fraction of 1 is filled with liquid whereas 0 means it is filled with gas. Any value in between represents the interface, which can be tracked using the Geo-reconstruct algorithm.

A variable time-step has been set to accelerate the calculation. The time-step should meet the CFL (i.e. Courant–Friedrichs–Levy) condition at any time as required by the explicit scheme used. The maximum value fixed for the CFL condition is 0.5 (Min and Park, 2011) giving a time-step of around 2.0e−05 s. PRESTO! and second-order upwind numerical schemes are selected for the discretization of pressure and momentum whereas the PISO scheme is used to perform the pressure–velocity coupling. Under-relaxation factors were used to ensure good convergence.

The computational domain consists of a 6 cm × 3 cm vertical plate similar to the one used previously by the authors (Sebastia-Saez et al., 2013). The structured mesh is formed by 579,852 hexahedral elements, with a higher density in the region next to the plate to better describe near-wall gradients. Both the schematic of the plate and a detail of the computational mesh can be seen in Fig. 1.

3. Theoretical background

3.1. Physical mass transfer

The physical absorption of CO_2 into the liquid film is implemented in the model by means of a source term UDF attached to the species transport equation. The source term according to Higbie's penetration theory follows Eq. (6), where the superscript (*) denotes saturation conditions:

$$S_{lg} = k_l a_e C_{l,TOT}(y_l^* - y_l) = k_g a_e C_{g,TOT}(y_g - y_g^*) \tag{6}$$

The concentration difference between the bulk phase and the interface (i.e. in which saturation conditions are assumed) constitutes the driving force of the absorption process. The saturation concentration is calculated with Henry's law. The gas-side mass transfer coefficient can be neglected as suggested in the literature. Sobieszuk and Pohorecki (2010) presented a comparative study of gas-side and liquid-side mass transfer coefficients for CO_2 absorption into falling liquid film micro-reactors. The authors concluded that for high CO_2 concentrations the mass transfer resistance on the gas-side resistance is several orders of magnitude lower than on the liquid-side (i.e. for pure absorbed gas k_g tends to an infinite value). Therefore, only the liquid-side mass transfer coefficient will be implemented in the present model, which according to the penetration theory can be calculated as:

$$k_l = 2\sqrt{\frac{D_l}{\pi\tau}} \tag{7}$$

Although some authors assumed that the change in CO_2 solubility as a function of the MEA weight percentage can be neglected (Wang et al., 2013), it is calculated in this work according to the methodology presented by Pentilä et al. (2011). The CO_2 diffusivity is calculated according to the Wilke–Chang equation (Wilke and Chang, 1955). The diffusivity and solubility of CO_2 cannot be measured properly in a reactive system. Therefore, a surrogate gas with analogous characteristics should be used instead of CO_2.

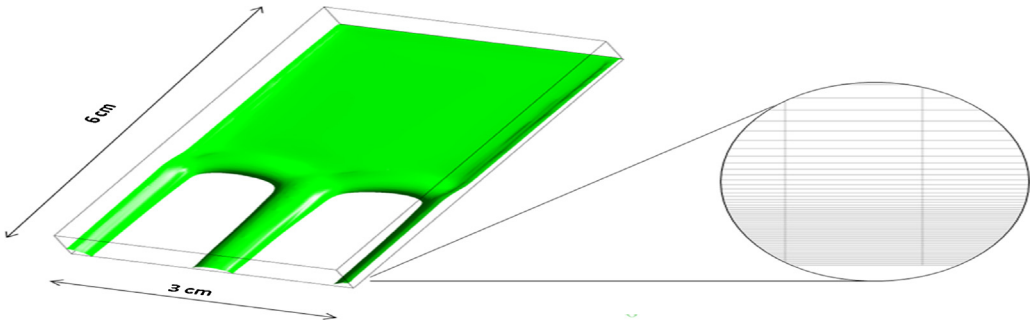

Fig. 1. Geometry and mesh details.

Table 2
Solubility, viscosity and diffusivity values.

MEA concentration (wt.%)	Viscosity (cP)	Solubility (g/l)	Diffusivity ($\times 10^{-5}$ cm^2/s)
30	7.9	1.06	0.41
40	10.2	1.09	0.31
50	12.5	1.14	0.26

The N_2O–CO_2 analogy is assumed for their calculation (Sema et al., 2012).

The viscosity of the MEA mixture is calculated with a mass weighted mixing law (i.e. 1 mPa s for pure water and 24 mPa s for pure MEA according to data provided by Dow® Chemical Company).

The values of the solubility, diffusivity and viscosity (i.e. at 20 °C) used in this study are presented in Table 2. MEA presents a similar value of the density compared to water (i.e. relative density equal to 1.0113).

The exposure time is computed as (Haroun et al., 2012):

$$\tau = \frac{L_i}{v_i} \tag{8}$$

The interfacial area per unit volume is computed as the gradient of the volume fraction (Xu et al., 2009).

$$a_e = |\nabla F_l| = |\nabla F_g| \tag{9}$$

3.2. Chemical system description

The CO_2-MEA chemical system is described by the zwitterion mechanism (Caplow, 1968; Danckwerts, 1979). The reaction mechanism is represented by the following set of reactions:

$$CO_2 + OH^- \rightleftharpoons HCO_3^- \tag{10}$$

$$CO_2 + MEA + H_2O \rightleftharpoons MEACOO^- + H_3O^+ \tag{11}$$

$$2H_2O \rightleftharpoons OH^- + H_3O^+ \tag{12}$$

$$HCO_3^- + H_2O \rightleftharpoons CO_3^{2-} + H_3O^+ \tag{13}$$

$$MEA + H_3O^+ \rightleftharpoons MEA^+ + H_2O \tag{14}$$

$$MEACOO^- + H_2O \rightleftharpoons MEA + HCO_3^- \tag{15}$$

In this process, the carbon dioxide reacts with the amine to form a zwitterion, which in turn reacts with the alkanolamine to form a carbamate. Reactions (12)–(15) are instantaneous whereas (10) and (11) have a finite rate and can be implemented in ANSYS® FLUENT by means of source term UDFs. Reaction (11) (i.e. carbamate formation) is the controlling step and describes the whole reaction kinetics. Reaction (10) can be neglected because of its slow kinetics (Faramarzi et al., 2010). Carbamate formation is a second order irreversible reaction and the reaction rate can be written as:

$$R = K_{for}[CO_2][MEA] \tag{16}$$

Where K_{for} is the forward reaction rate. The value presented by Kale et al. (2013) [K_{for} = 24,984 m^3 kmol$^{-1}\cdot^{-1}$] is implemented in the present simulation. For a second order irreversible reaction, van Krevelen and Hoftijzer (1948) calculated the enhancement factor, which is given as:

$$E = \frac{\sqrt{M((E_\infty - E)/(E_\infty - 1))}}{\tanh\left(\sqrt{M((E_\infty - E)/(E_\infty - 1))}\right)} \tag{17}$$

In Eq. (17) M is equal to the squared Hatta number and E_∞ is the enhancement factor for instantaneous irreversible reaction, which is a function of the diffusivities and concentrations of both MEA and CO_2:

$$E_\infty = \sqrt{\frac{D_{CO_2}}{D_{MEA}}}\left(1 + \frac{D_{MEA}\, c_{MEA}}{zD_{CO_2}\, c_{CO_2,i}}\right) \tag{18}$$

The equation for the Hatta number reads (Hikita and Asai, 1964):

$$Ha = \frac{\sqrt{(2/(m+1))k_{m,n}[CO_2]^{m-1}[MEA]^n D_{CO_2,l}}}{k_l} \tag{19}$$

Where $k_{m,n}$ is the reaction rate constant. In this case $m, n = 1$ and the aforementioned definition can be simplified to:

$$Ha = \frac{\sqrt{k_2[MEA]D_{CO_2,l}}}{k_l} \tag{20}$$

Ha compares the reaction and the solute diffusion rate and can be used to indicate whether the reaction takes place either in the bulk phase or only in the gas–liquid interface. A higher Hatta number implies that the chemical reaction is more dominant with respect to the physical absorption process whereas the opposite occurs when its value is low.

The Hatta number is also closely related to the enhancement factor, which is the ratio between the absorption rate with and without chemical reaction. The enhancement factor gives a notion on how the existence of the chemical reaction can intensify the absorption process.

Three reaction regimes can be found in the literature depending on the relationship between the enhancement factor and the Hatta number. The reaction regimes are established as follows (Kale et al., 2013):

- For $Ha < 1$ the reaction is slow compared to the diffusive process and it occurs in both the bulk phase and the gas–liquid interface.

Table 3
Enhancement factor calculation approaches.

Approximation	Conditions	Enhancement factor
Instantaneous reaction	$Ha > 10\,E_i$	$E = E_i$
Pseudo-first order	$Ha < 1/2\,E_i$	$E = \frac{Ha}{\tanh(Ha)}$
Second order irreversible	General case	Eq. (17)

The enhancement factor is approximately 1, which implies that the absorption process is not affected by the reaction.

- For $1 < Ha < 10$ the reaction takes place in both the interface and the liquid film. In this regime, the rate of mass transfer in the liquid film depends on the reaction rate and diffusion flux. The trend linking both the Hatta number and the enhancement factor can be approximated to a pseudo-first order behavior. The enhancement factor can be calculated as shown in Table 3.
- When $Ha > 10$, the reaction is much faster than the diffusion process. The depletion of the solute in the bulk phase occurs and the enhancement factor is constant as Ha increases. Under these circumstances the rate of absorption depends completely on the diffusivity of the reacting components. If the MEA concentration is high enough (i.e. $\tanh(Ha) \cong 1$) then the enhancement factor is approximately equal to Ha. The reaction behavior is thus similar to a first order behavior hence fast pseudo-first order (Wilcox et al., 2014). A further MEA concentration increase would give an instantaneous behavior. The enhancement factor is in this case approximated to E_∞.

The enhancement factor is calculated in a different way depending on the value of the Hatta number associated to the reaction. Table 3 summarizes the different formulae used:

For the high MEA concentrations found in industry and reproduced in this work, fast pseudo-first order conditions are met (i.e. $Ha > 10$). The enhancement factor is thus approximately equal to the Hatta number.

The enhancement factor is introduced in Eq. (6) to represent the increase in the absorption rate ascribed to the chemical reaction. The source term for the reactive absorption is thus rewritten as:

$$S_{lg} = E k_l a C_{TOT} y_l^* \tag{21}$$

Where the CO_2 concentration in the bulk phase has been neglected according to the fact that the solute is depleted in the bulk phase.

The CO_2 concentration profiles obtained with the different kinetics approaches as well as the effect of the reversibility of the reaction are analyzed in this work. Also the influence of both the MEA concentration and the liquid velocity using the present models is assessed in the next section.

4. Results

4.1. Hydrodynamics of the aqueous MEA solution

The validation of the hydrodynamics of a liquid film flowing along an inclined plate was accomplished in our previous work (Sebastia-Saez et al., 2013). The wetted area as a function of the Reynolds number for the case of pure water was compared to the experimental results presented by Hoffmann et al. (2005) and Iso et al. (2013), showing a satisfactory agreement. Three different liquid film shapes depending on the value of the liquid injection velocity (i.e. trickling, rivulet and full film flow) were observed and explained by means of the Weber number (i.e. ratio between distortive and cohesive forces):

$$We = \frac{\rho v^2 \delta}{\sigma} \tag{22}$$

Distortive forces (i.e. mainly inertia) tend to spread the liquid along the plate whereas cohesive forces (i.e. surface tension) tend to reduce the gas–liquid interface. A reduction in the interfacial area available for mass exchange is thus observed for low values of the Webber number, causing a diminishing on the absorption rate. On the other hand, higher values for the liquid injection velocity help spreading the liquid over the plate, enhancing the absorption process. However, not only inertia and surface tension have an influence on the amount of wetted area. Also the liquid–solid adhesion and the liquid cohesion (i.e. which translates into different values of the liquid–solid contact angle) can affect the liquid spreading (Sebastia-Saez et al., 2014).

The same model was extended thereafter to implement physical mass transfer of oxygen into water in a later article. Subsequently, the validated hydrodynamic and mass transfer models are applied in this work to describe the chemical absorption of CO_2 using amine solutions. The present work implements the liquid flow of commercial water–amine mixtures used in industry (i.e. 30%, 40%, and 50 wt.% MEA). Fig. 2 shows the evolution of the wetted area with flow time for the three MEA solutions and pure water with $\nu = 38\,\mathrm{cm\ s^{-1}}$ at the liquid inlet boundary. It is found that a substantial variation in the hydrodynamics behavior of the liquid film occurs for an aqueous amine solution compared to water (i.e. it takes up to 1.7 s to reach pseudo-steady state depending on MEA concentration). The development of the liquid film flow presents three stages. In the first one, the covered area increases rapidly until the lateral rivulets reach the outlet. The second stage, which begins approximately after 0.3 s flow time, is characterized by the advance of the front wave until all the surface of the plate is covered by the liquid. The second stage, which was not observed for the case of pure water, is caused by the high viscosity of the amine. For pure water, there is no progress of the front wave after the lateral rivulets reach the outlet and the second stage is therefore suppressed. The third stage corresponds to the full film flow regime, which is reached after approximately 1.3 s flow time. Fig. 3 helps to visualize the liquid film development, showing a snapshot of each flow development stage for the base case of a 30 wt.% amine solution and liquid injection velocity of $38\,\mathrm{cm\,s^{-1}}$. The results in Fig. 2 show a similar film flow development for the amine solutions due to the relatively small difference in viscosity between them (i.e. see Table 2) if compared to pure water. In fact, an increase in viscosity of 29% and 22.5% is found when the MEA contents rises from 30 wt.% to 40 wt.% and from 40 wt.% to 50 wt.% respectively whereas the viscosity of the 30 wt.% MEA solution is eight times bigger than that of water. However, the general trend shows that a lower viscosity gives a slightly higher wetted area during the first and second stages while reducing the time required to reaching full film flow. The difference is more appreciable when compared to water, which has a low viscosity value with respect to the amine solutions. Therefore, it has been observed that, when the viscosity is low, the liquid does not cover the plate totally once pseudo-steady conditions are reached. For the case of an amine solution, the wetted area evolution in time is slower by virtue of the high viscosity and it ends up by covering the entire plate. Dependence between the wettability and both the liquid injection velocity and viscosity is thus observed.

The velocity profiles within the liquid film are compared with Nusselt theory, showing a reasonable match (Fig. 4). The graph shows the profiles for the case with 30 wt.% MEA aqueous solution with $38\,\mathrm{cm\,s^{-1}}$ liquid injection velocity. The equation for the velocity profile reads (Nusselt, 1916):

$$v(z) = \frac{\rho_l g \delta^2 \sin(\beta)}{2\mu_l}\left[1 - \left(\frac{z}{\delta}\right)^2\right] \tag{23}$$

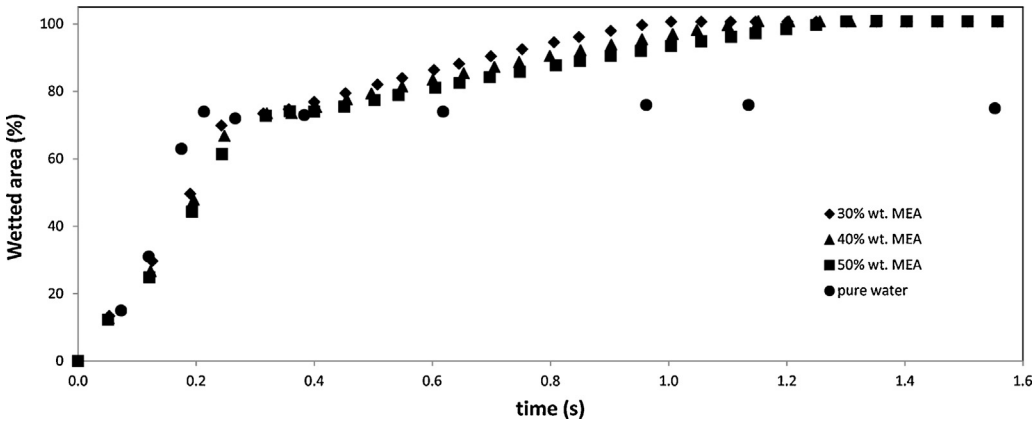

Fig. 2. Time dependent evolution of wetted area.

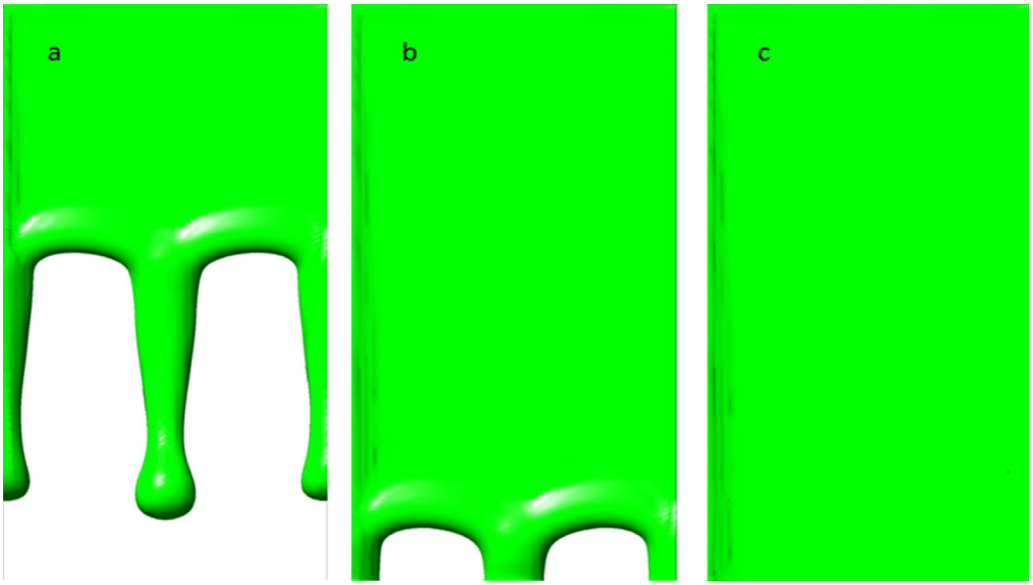

Fig. 3. Liquid film development at (a) 0.2 s, (b) 0.9 s, and (c) 1.5 s.

Fig. 5 compares the velocity profiles for the amine solutions. A more viscous solution (i.e. higher amine percentage) presents a lower velocity value at the interface and a higher film thickness as it can be seen in the y and x axes respectively. This behavior can be explained by Nusselt theory, which predicts lower velocity values and thicker liquid films as the viscosity increases. The relationship between the velocity and the liquid film thickness as a function of the MEA mass fraction would also explain the slower development of the liquid film. As a consequence, the wetted area increases faster with time for the least viscous fluid by virtue of its higher velocity as observed in Fig. 2.

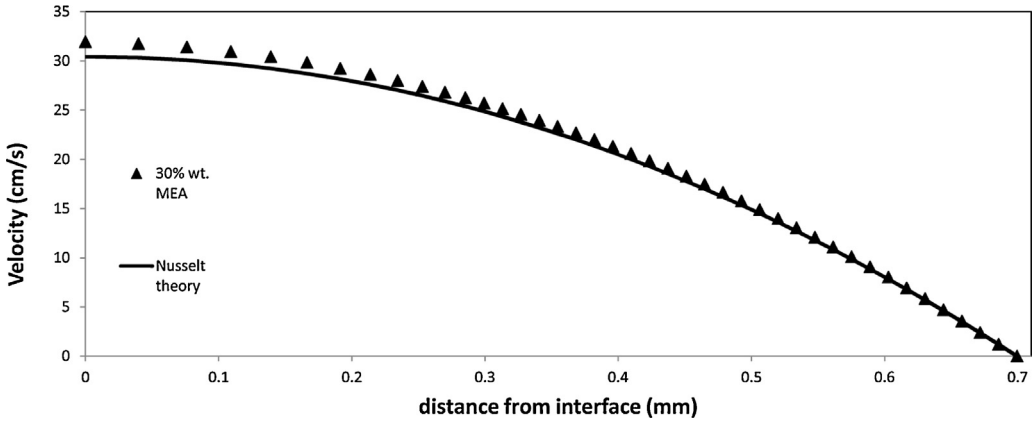

Fig. 4. Theoretical and CFD velocity profile (30 wt.% MEA).

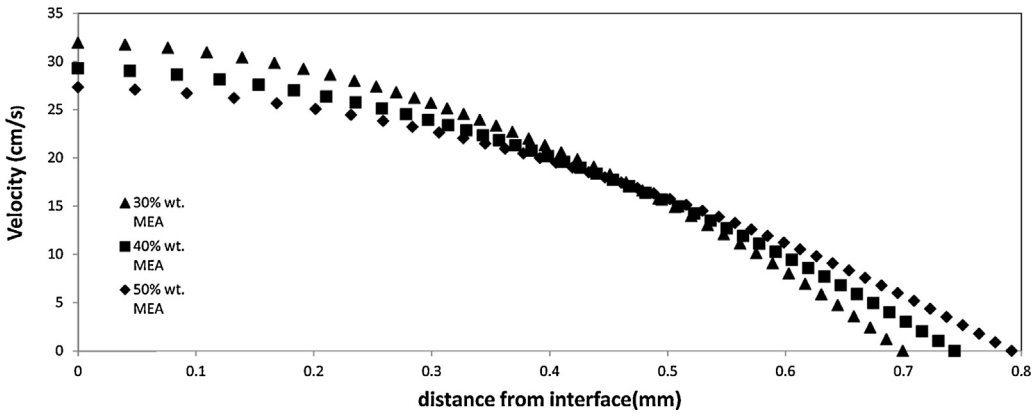

Fig. 5. Velocity profiles and liquid film thickness for the three amine solutions tested.

Table 4
Enhancement factor and liquid film thickness results.

MEA wt.%	Liquid film thickness (μm)	E (from simulation)
30	699	76.94
40	743	91.49
50	792	104.47

4.2. Influence of MEA concentration on the enhancement factor

Fig. 6 shows the variation of the enhancement factor as a function of the MEA mass fraction once pseudo-steady state is reached. The increasing tendency can be explained by the fact that the enhancement factor is equal to the value of the Hatta number of the chemical system, which is proportional, in turn, to the squared root of the amine concentration in the aqueous solution. Thus, the enhancement factor has necessarily to depend directly on the MEA contents. An increase in the MEA concentration leads therefore to an increase in the enhancement factor when the assumption of $E \cong Ha$ is taken as it is observed in Fig. 6 (i.e. assumption applied for the case of the carbamate formation reaction that has been modeled in this work). The physical reason why the chemical reaction is enhanced when the MEA concentration increases is because the probability of collision between the reactant molecules to trigger the reaction is higher, as explained by the kinetic theory.

A higher amine concentration also affects the liquid-side mass transfer coefficient as it can be observed in Fig. 7. Higher amine concentrations result in an increased viscosity of the solution, which reduces the value of the CO_2 diffusivity through the liquid phase as shown in Table 2. The Hatta number is inversely proportional to the liquid-side mass transfer coefficient, which in turn depends directly on the diffusivity. Therefore, it can be concluded that increasing the amine concentration enhances the reactive mass transfer process in two ways: affecting the probability of the reaction to occur and reducing the diffusivity of the gas in the liquid phase. This tendency is generally widespread in literature and has been already predicted in process simulations. The order of magnitude of the enhancement factors obtained in this work is also in agreement with reported data from Liu et al. (2006), who showed values ranging from 30 to 150 depending on the distance to the bottom of the column.

Further evidence of this behavior is also reported by Meldon and Morales-Cabrera (2011), who study the influence of the liquid film thickness in the enhancement factor, showing a direct relationship between them. The authors found that increasing the amine concentration in the liquid phase causes an increase in the viscosity of the solution, which in turn results in thicker liquid films and bigger enhancement factors.

Table 4 includes the values of liquid film thickness found in this work and their associated enhancement factors. The results show the same tendency reported by Meldon and Morales-Cabrera (2011). It can be also observed in Table 4 that when the MEA concentration passes from 30 wt.% to 40 wt.% the enhancement factor is increased from approximately 77 to 91, which means a 15% increase. Further increase in MEA concentration from 40 wt.% to 50 wt.% results in a CO_2 absorption enhancement rise from about 91 to 104, with a 12.5% of enhancement achieved.

As a conclusion, it must be said that the CO_2 absorption capacity rises (i.e. through augmenting the enhancement factor) with the amine concentration. However, the difference becomes smaller as the MEA contents increases.

The liquid load also influences the enhancement factor as it can be observed in Fig. 6. Two values of the liquid load have been tested (i.e. 38 cm s^{-1} and 45 cm s^{-1}). As a general trend, a larger liquid load gives lower enhancement factors, with a constant difference of about 8% with respect to the base case of 38 cm s^{-1}. This can be explained by the fact that higher liquid loads give lower values of the film thickness hence higher liquid velocities, which influence the liquid side mass transfer coefficient through Eqs. (7) and (8). Bigger liquid film velocity values give lower exposure times (Eq. (8)), which result in an increase in the liquid-side mass transfer coefficient. The Hatta number is inversely proportional to k_l (Eq. (20)) hence the trend shown in Fig. 6.

4.3. Influence of MEA concentration on the CO_2 concentration profiles

The carbon dioxide profiles within the liquid film are presented in this section. Fig. 8 shows the CO_2 concentration profiles in the liquid phase for different MEA concentration values. It is important to note that the amount of dissolved CO_2 should not be confused with the amount absorbed by the solution from the gas phase due to the fact that part of the CO_2 is consumed by the reaction, forming the carbamate. It is observed that the CO_2 concentration is higher for the lower MEA concentration values. This behavior can be explained by the increase in the CO_2 diffusivity and the lower reaction rates that exist when the MEA concentration decreases. It can also be observed that the saturation conditions (~106 mmol/l) are not reached owing to the small contact time ($\tau < 1\,s$) between both phases. The maximum dissolved CO_2 concentration obtained is 0.15, 0.05, 0.04 mmol/l, for 30%, 40%, 50 wt.% amine concentration respectively. By increasing the amine contents, a decrease in the CO_2 concentration appears as a consequence of the chemical reaction as shown in Fig. 8. It is also found that the penetration depth of the dissolved CO_2 in the bulk liquid does not exceed 0.1 mm in any case because of its depletion in the bulk liquid phase.

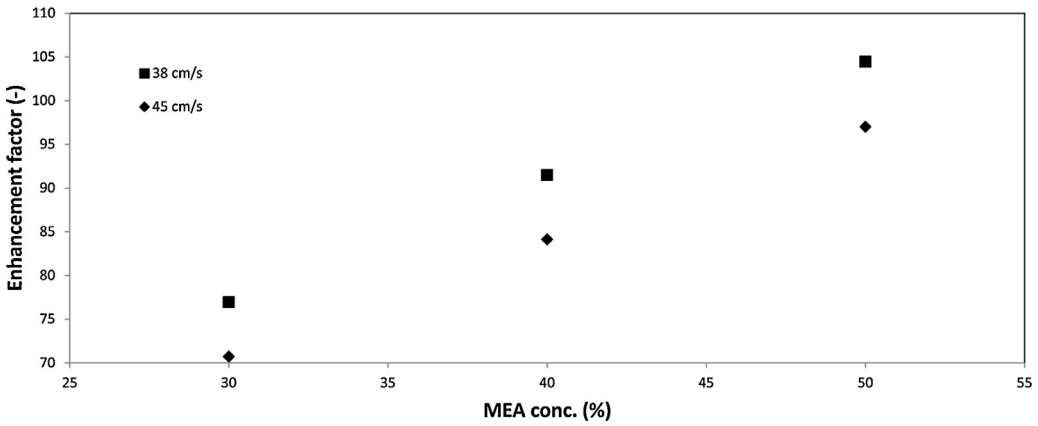

Fig. 6. Enhancement factor vs. MEA conc.

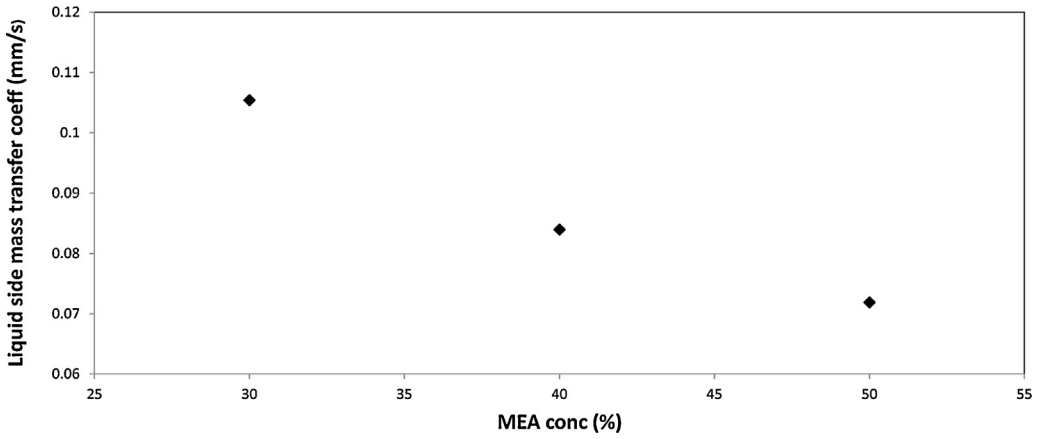

Fig. 7. Liquid side mass transfer coefficient vs. MEA conc.

The calculated reaction source terms for all species are equal to zero in the bulk phase considering the fast reaction kinetics. The model is thus able to reproduce the fact that the reaction takes place strictly in the gas–liquid interface as it is suggested by theory when $Ha > 10$.

Fig. 9 shows the concentration profiles as a function of the contact time for the base case with 30 wt.% MEA and 38 cm s^{-1} (i.e. 26 ms, 79 ms, and 132 ms). The contact time depends on the distance from the liquid inlet. Higher CO_2 concentration values might be expected as contact time increases. However, the enhancement factor also increases with the distance from the liquid inlet as it has been reported in the literature. The chemical reaction becomes thus more important as contact time increases, which results in the lower values of the CO_2 concentration found in these simulations.

Fig. 10 shows the comparison between the CO_2 concentration profiles with and without chemical reaction. For the physical absorption case, the results are obtained by disabling the consumption source terms. The penetration depth for chemical absorption is around 0.1 mm whereas a significant concentration of CO_2 is found along the whole liquid film thickness for the case of physical absorption owing to the fact that the non-existence of the chemical reaction allows diffusion to take place. The maximum dissolved CO_2 concentration obtained for physical absorption is 0.586 mmol/l

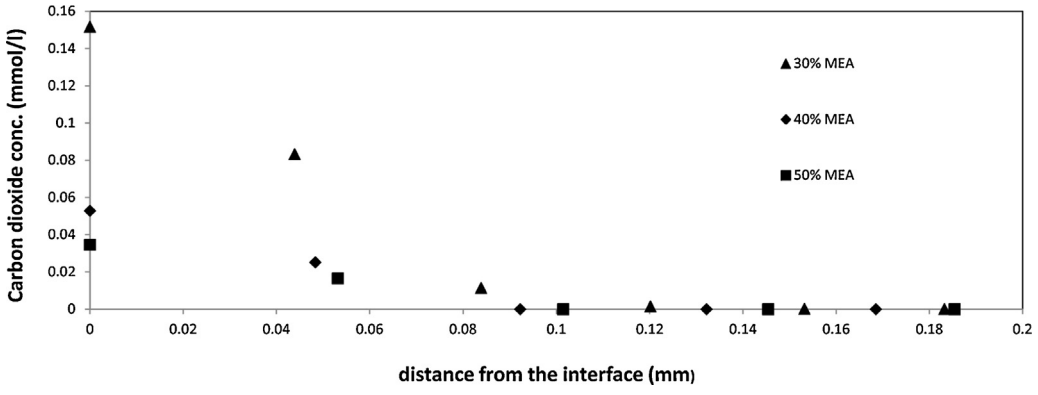

Fig. 8. CO_2 concentration profile for three different amine solutions.

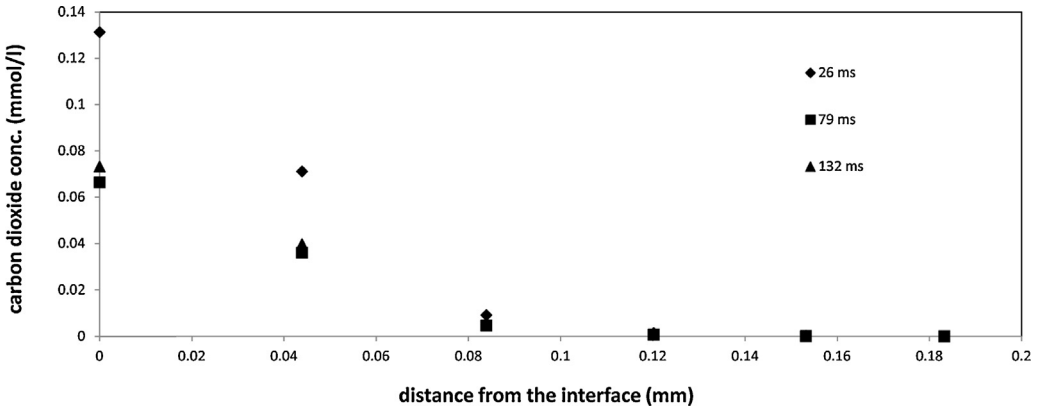

Fig. 9. Concentration profiles for different values of the contact time.

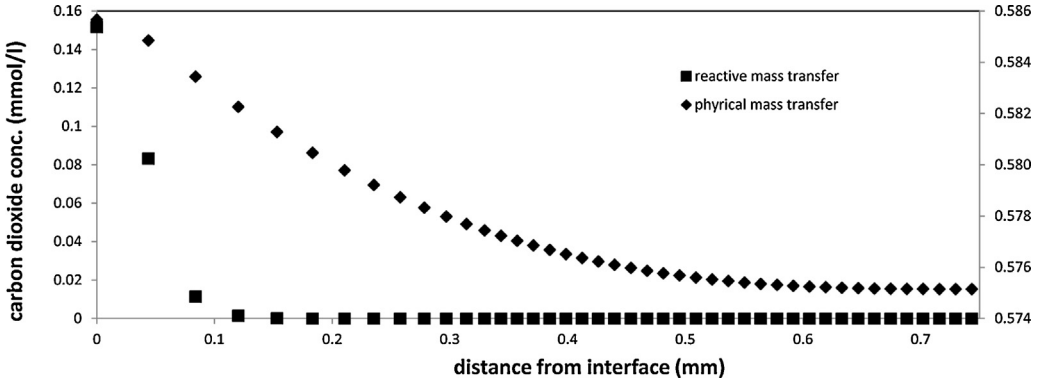

Fig. 10. Concentration profile with and without chemical reaction (30 wt.% MEA).

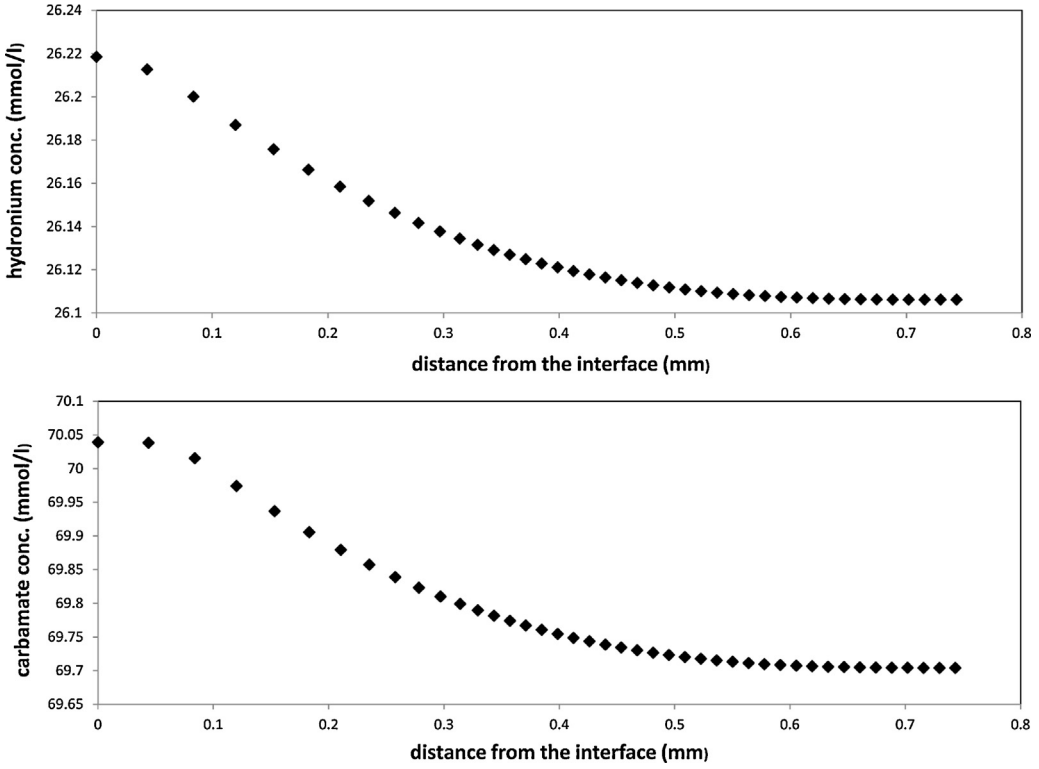

Fig. 11. Hydronium (a) and carbamate (b) concentration profiles.

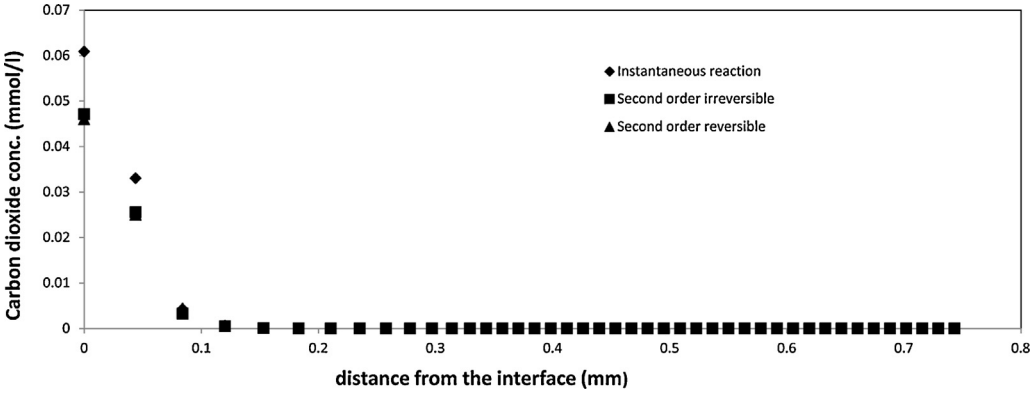

Fig. 12. Concentration profiles depending on the chemical reaction scheme approach.

Table 5
Chemical absorption parameters for the three cases tested.

Reaction approach	E	Reaction rate [kg m^{-3} s^{-1}]	Absorption rate [kg m^{-3} s^{-1}]
Second order reversible	114.7	0.57	32.9
Second order irreversible	114.8	0.57	33.0
Instantaneous reaction	186.7	0.95	49.0

whereas it is 0.15 mmol/l for chemical absorption with 30 wt.% MEA concentration. Higher concentration values along the liquid film thickness for the physical absorption case are also in accordance with the existence or not of the chemical reaction. The model is thus capable of describing that the CO_2 penetrates into the liquid film through the gas–liquid interface and is consumed while trying to reach the bulk liquid. The consumption of carbon dioxide helps keeping a high concentration gradient between both phases, which favors enhanced carbon dioxide absorption rates.

Fig. 11 shows the concentration profiles of the reaction products (i.e. both hydronium and carbamate are represented). The profiles show a trend similar to the CO_2 concentration profile obtained without chemical reaction by virtue of diffusion through the liquid film. The variation of water and MEA concentration are not plotted in this figure because of its negligible value (i.e. the MEA concentration in the liquid phase is considerably bigger than the stoichiometric value). As a conclusion, CO_2 is the only species that is present only in the gas–liquid interface as a result of its depletion in the bulk liquid.

4.4. Effect of different kinetics approaches on the CO_2 absorption behavior

Fig. 12 presents the CO_2 concentration obtained for three different approaches for the reaction kinetics. Second order, with and without reversibility of the reaction, and the instantaneous approach are represented. The carbamate formation is a fast reaction that can be approximated as instantaneous hence the similar results between the three approaches. The reaction kinetics presents reversibility but its effect can be neglected (i.e. high Hatta number) according to the literature. The results from both reversible and irreversible second order are identical as seen in Fig. 12 for the base case with 30 wt.% MEA. The model is thus able to describe that the effect of the reversibility is negligible. Furthermore, the carbamate formation can be approximated to an instantaneous reaction when the amine concentration is high as it happens in industry. This causes that similar values for the carbon dioxide profiles are obtained regardless of which one of the three approaches is implemented. Table 5 shows the results obtained for the enhancement factor, the reaction rate and the absorption rate. The gain in the absorption rate is explained by the fact that a higher enhancement factor gives more gas–liquid mass transfer rates through Eq. (21). The enhanced reaction rates can be explained by the existence of a bigger amount of carbon dioxide dissolved in the liquid phase.

5. Conclusions

A micro-scale CFD model to describe CO_2 reactive absorption into aqueous MEA in falling liquid films has been developed. The carbamate formation reaction has been considered as the controlling step of the whole chemical system. The hydrodynamics of the high viscosity liquid films have been studied, showing substantial differences in the time-dependent evolution of the falling liquid film formation for the aqueous amine solutions when compared to water. Thicker liquid films have also been found when the MEA concentration increases as suggested by Nusselt theory. The velocity profiles also match the theoretical predictions. The variation of the enhancement factor with the amine concentration follows an increasing tendency, which is in agreement with the reported trends found in the literature. The CO_2 concentration profiles within the liquid film have also been analyzed. A higher concentration of CO_2 is found for lower values of the MEA percentage, which is explained by a higher diffusivity and lower reaction rates. The model is also capable of reproducing the depletion of carbon dioxide in the liquid bulk, which is in accordance with the value of the Hatta number associated to the MEA–CO_2 chemical system. The concentration profiles with and without chemical reaction are also used to highlight the solute depletion in the liquid region far from the interface. Lower values of the concentration are obtained all over the liquid film for the reactive absorption case because of the consumption of CO_2 during the mass transfer process from the gas phase into the liquid bulk.

Finally, the three approximations for the value of the Hatta number shown in Table 5 are tested, showing that the effect of the reversibility can be neglected. The assumption of an instantaneous reaction presents similar values but it fails at matching the results obtained for the second order reaction kinetics. An increase in the amount of carbon dioxide dissolved is observed when the reaction is considered as instantaneous, which is explained by a higher value of the enhancement factor. As a general conclusion, the second order irreversible approach is suitable to explain the CO_2 reactive absorption process occurring within a structured packing column since the conditions mentioned in Table 3 are met. This work aims to fill the gap on reactive mass transfer CFD modeling detected in the literature and can be used in the future to optimize the performance of structured packing materials.

Acknowledgements

The authors gratefully acknowledge the financial support for this work by the UK Engineering and Physical Sciences Research Council (EPSRC) project grant: EP/J020184/1 and FP7 Marie Curie iComFluid project grant: 312261.

References

Ahn, H., Luberti, M., Liu, Z., Brandani, S., 2013. Process simulation of aqueous MEA plants for post-combustion capture from coal-fired power plants. Energy Procedia 37, 1523–1531.

Brackbill, J.U., Kothe, D.B., Zemach, C., 1992. A continuum method for modelling surface tension. J. Comput. Phys. 100, 335–354.

Brinkmann, U., Janzen, A., Kenig, E.Y., 2014. Hydrodynamic analogy approach for modelling reactive absorption. Chem. Eng. J. 250, 342–353.

Buba, P., Kumar, R., Linga, P., 2013. Pre-combustion capture of carbon dioxide in a fixed bed reactor using the clathrate hydrate process. Energy 50, 364–373.

Caplow, M., 1968. Kinetics of carbamate formation and breakdown. J. Am. Chem. Soc. 90, 6795–6803.

Chen, J., Liu, C., Yuan, X., Yu, G., 2009. CFD simulation of flow and mass transfer in structured packing distillation columns. Chin. J. Chem. Eng. 17, 381–388.

Cooke, J.J., Armstrong, L.M., Luo, K.H., Gu, S., 2014. Adaptive mesh refinement of gas–liquid flow on an inclined plane. Comput. Chem. Eng. 60, 297–306.

Danckwerts, P.V., 1979. The reaction of CO_2 with ethanolamines. Chem. Eng. Sci. 34, 443–446.

Edge, P.J., Heggs, P.J., Pourkashanian, M., Stephenson, P.L., 2013. Integrated fluid dynamics-process modelling of a coal-fired power plant with carbon capture. Appl. Therm. Eng. 60, 456–464.

Fagerlund, F., Niemi, A., Bensabat, J., Shtivelman, V., 2013. Design of a two-well field test to determine in situ residual and dissolution trapping of CO_2 applied to the Heletz CO_2 injection site. Int. J. Greenh. Gas Control 19, 642–651.

Faramarzi, L., Kontogeorgis, G.M., Michelsen, M.L., Thomsen, K., Stenby, E.H., 2010. Absorber model for CO_2 capture by monoethanolamine. Ind. Eng. Chem. Res. 49, 3751–3759.

Haroun, Y., Legendre, D., Raynal, L., 2010. Volume of fluid method for interfacial reactive mass transfer: application to stable liquid film. Chem. Eng. Sci. 65, 2896–2909.

Haroun, Y., Raynal, L., Legendre, D., 2012. Mass transfer and liquid hold-up determination in structured packing by CFD. Chem. Eng. Sci. 75, 342–348.

Haroun, Y., Raynal, L., Alix, P., 2014. Prediction of effective area and liquid hold-up in structured packings by CFD. Chem. Eng. Res. Des., http://dx.doi.org/10.1016/j.cherd.2013.12.029.

Hikita, H., Asai, S., 1964. Gas absorption with (m,n)-th order irreversible chemical reaction. Int. Chem. Eng. 9 (4), 332–340.

Hoffmann, A., Ausner, I., Repke, J.U., Wozny, G., 2005. Fluid dynamics in multiphase distillation processes in packed towers. Comput. Chem. Eng. 29, 1433–1437.

Hosseini, S.H., Shojaee, S., Ahmadi, G., Zivdar, M., 2012. Computational fluid dynamics studies of dry and wet pressure drops in structured packings. J. Ind. Eng. Chem. 18, 1465–1473.

Iso, Y., Huang, J., Kato, M., Matsuno, S., Takano, K., 2013. Numerical and experimental study on liquid film flows on packing elements in absorbers for post-combustion CO_2 capture. Energy Procedia 37, 860–868.

Kale, C., Górak, A., Schoenmakers, H., 2013. Modelling of the reactive absorption of CO_2 using mono-ethanolamine. Int. J. Greenh. Gas Control 17, 294–308.

Liovic, P., Lakehal, D., 2012. Subgrid-scale modelling of surface tension within interface tracking-based Large Eddy and Interface Simulation of 3D interfacial flows. Comput. Fluids 63, 27–46.

Liu, G.B., Yu, K.T., Yuan, X.G., Liu, C.J., Guo, Q.C., 2006. Simulations of chemical absorption in pilot-scale and industrial-scale packed columns by computational mass transfer. Chem. Eng. Sci. 61, 6511–6529.

Meier, M., Yadigaroglu, G., Smith, B.L., 2002. A novel technique for including surface tension in PLIC-VOF methods. Eur. J. Mech. B: Fluids 21, 61–73.

Meldon, J.H., Morales-Cabrera, M.A., 2011. Analysis of carbon dioxide absorption in and stripping from aqueous monoethanolamine. Chem. Eng. J. 171, 753–759.

Min, J.K., Park, I.S., 2011. Numerical study for laminar wavy motions of liquid film flow on vertical wall. Int. J. Heat Mass Transfer 54, 3256–3266.

Mores, P., Rodríguez, N., Scenna, N., Mussati, S., 2012. CO_2 capture in power plants: minimization of the investment and operating cost of the post-combustion process using MEA aqueous solution. Int. J. Greenh. Gas Control 10, 148–163.

Nusselt, W., 1916. Die oberflächenkondensation des wasserdampfes. Z. Ver. Dtsch. Ing. 60, 541–546.

Odenberger, M., Johnson, F., 2010. Pathways for the European electricity supply system to 2050 – the role of CCS to meet stringent CO_2 reduction targets. Int. J. Greenh. Gas Control 4, 327–340.

Pentilä, A., Dell'era, C., Uusi-Kyyny, P., Alopaeus, V., 2011. The Henry's law constant of N_2O and CO_2 in aqueous solutions (MEA, DEA, DIPA, MDEA, and AMP). Fluid Phase Equilib. 311, 59–66.

Power, H., 2011, July 20. LLNL, CERI Partner for Clean Energy R&D (R&D).

Raynal, L., Bouillon, P.A., Gomez, A., Broutin, P., 2011. From MEA to demixing solvents and future steps, a roadmap for lowering the cost of post-combustion carbon capture. Chem. Eng. J. 171, 742–752.

Raynal, L., Royon-Lebeaud, A., 2007. A multi-scale approach for CFD calculations of gas–liquid flow within large size column equipped with structured packing. Chem. Eng. Sci. 62, 7196–7204.

Romeo, L.M., Bolea, I., Escosa, J.M., 2008. Integration of power plant and amine scrubbing to reduce CO_2 capture cost. Appl. Therm. Eng. 28, 1039–1046.

Said, A., Eloneva, S., Fogelholm, C.J., Fagerlund, J., Nduagu, E., Zevenhoven, R., 2011. Integrated carbon capture and storage for an oxyfuel combustion process by using carbonation of $Mg(OH)_2$ produced from serpentinite rock. Energy Procedia 4, 2839–2846.

Sebastia-Saez, D., Gu, S., Ranganathan, P., Papadikis, K., 2013. 3D modeling of hydrodynamics and physical mass transfer characteristics of liquid film flows in structured packing elements. Int. J. Greenh. Gas Control 19, 492–502.

Sebastia-Saez, D., Gu, S., Ranganathan, P., Papadikis, K., 2014. Micro-scale CFD study about the influence of operative parameters on physical mass transfer within structured packing elements. Int. J. Greenh. Gas Control 28, 180–188.

Sema, T., Naami, A., Fu, K., Edali, M., Liu, H., Shi, H., Liang, Z., Idem, R., Tontiwachwuthikul, P., 2012. Comprehensive mass transfer and reaction kinetics studies of CO_2 absorption into aqueous solutions of blended MDEA–MEA. Chem. Eng. J. 209, 501–512.

Sobieszuk, P., Pohorecki, R., 2010. Gas-side mass transfer coefficients in a falling film microreactor. Chem. Eng. Process. 49, 820–824.

Sun, B., He, L., Liu, B.T., Gu, F., Liu, C.J., 2013. A new multi-scale model based on CFD and macroscopic calculation for corrugated structured packing column. AIChE J. 59, 3119–3130.

van Krevelen, D.W., Hoftijzer, P.J., 1948. Kinetics of gas–liquid reactions. Part I: general theory. Recl. Trav. Chim. Pays-Bas 67, 563–586.

Wang, M.H., Ledoux, A., Estel, L., 2013. Oxygen solubility measurements in a $MEA/H_2O/CO_2$ mixture. J. Chem. Eng. Data 58, 1117–1121.

Wilcox, J., Rochana, P., Kirchofer, A., Glatz, G., He, J., 2014. Revisiting film theory to consider approaches for enhanced solvent-process design for carbon capture. Energy Environ. Sci. 7, 1769–1785.

Wilke, C.R., Chang, P., 1955. Correlation of diffusion coefficients in dilute solutions. AIChE J. 1, 264–270.

Xu, Y., Paschke, S., Repke, J.U., Yuan, J.Q., Wozny, G., 2009. Computational approach to characterize the mass transfer between the counter-current gas–liquid flow. Chem. Eng. Technol. 32, 1227–1235.